LETTER

doi:10.1038/nature11253

Gate-tuning of graphene plasmons revealed by infrared nano-imaging

Z. Fei[1], A. S. Rodin[1], G. O. Andreev[1], W. Bao[2,3], A. S. McLeod[1], M. Wagner[1], L. M. Zhang[4], Z. Zhao[2], M. Thiemens[5], G. Dominguez[6], M. M. Fogler[1], A. H. Castro Neto[7], C. N. Lau[2], F. Keilmann[8] & D. N. Basov[1]

Surface plasmons are collective oscillations of electrons in metals or semiconductors that enable confinement and control of electromagnetic energy at subwavelength scales[1–5]. Rapid progress in plasmonics has largely relied on advances in device nano-fabrication[5–7], whereas less attention has been paid to the tunable properties of plasmonic media. One such medium—graphene—is amenable to convenient tuning of its electronic and optical properties by varying the applied voltage[8–11]. Here, using infrared nano-imaging, we show that common graphene/SiO_2/Si back-gated structures support propagating surface plasmons. The wavelength of graphene plasmons is of the order of 200 nanometres at technologically relevant infrared frequencies, and they can propagate several times this distance. We have succeeded in altering both the amplitude and the wavelength of these plasmons by varying the gate voltage. Using plasmon interferometry, we investigated losses in graphene by exploring real-space profiles of plasmon standing waves formed between the tip of our nano-probe and the edges of the samples. Plasmon dissipation quantified through this analysis is linked to the exotic electrodynamics of graphene[10]. Standard plasmonic figures of merit of our tunable graphene devices surpass those of common metal-based structures.

In general, surface plasmons can exist in any material with mobile charge carriers whose response to electric field remains reactive—that is, whose in-plane momentum (q)-dependent and frequency (ω)-dependent complex conductivity, $\sigma(q,\omega) = \sigma_1 + i\sigma_2$, is predominantly imaginary. Of particular interest are plasmons with high momenta, $q_P \gg \omega/c$ (where c is the velocity of light), which may be used for extreme concentration of electromagnetic energy[1–5]. In conventional bulk metals, the frequencies of such high-q plasmons reside in the visible or ultraviolet ranges. In graphene, they are expected to appear in the terahertz and infrared domains[12]. However, these high-q infrared plasmons are dormant in conventional spectroscopy of graphene. Here we used the scattering-type scanning near-field optical microscope (scattering-type SNOM) to experimentally access high-q plasmons by illuminating the sharp tip of an atomic force microscope (AFM) with a focused infrared beam (Fig. 1a). The momenta imparted by the tip extend up to a few times $1/a$, where $a \approx 25$ nm is the curvature radius of the tip[13], thus spanning the typical range of infrared plasmon momenta (q_P) in graphene[12]. The spatial resolution of scattering-type SNOM is also set by a, and proves to be an order of magnitude smaller than the plasmon wavelength λ_P. The direct observable of our method—the scattering amplitude $s(\omega)$—is a measure of the electric field strength inside the nanoscale gap between tip and sample. Consequently, the scattering-type SNOM technique enables spectroscopy[13] and infrared nano-imaging of graphene plasmons without the need to fabricate specialized periodic structures[14]. Our imaging data elucidate real-space characteristics of infrared plasmons in graphene such as reflection, interference and damping. All these phenomena can be readily manipulated with gate voltage—a noteworthy property unattainable in metal-based plasmonics.

To probe directly the properties of graphene plasmons, we utilize a frequency $\omega = 892\ cm^{-1}$ corresponding to a wavelength $\lambda_{IR} = 11.2\ \mu m$ in the infrared (IR) regime where the plasmon is unimpeded by the surface optical phonon supported in graphene/SiO_2/Si structures[13]. The nano-imaging results are shown in Fig. 1b–e, where we plot normalized near-field amplitude $s(\omega) = s_3(\omega)/s_3^{Si}(\omega)$. Here $s_3(\omega)$ and $s_3^{Si}(\omega)$ are the

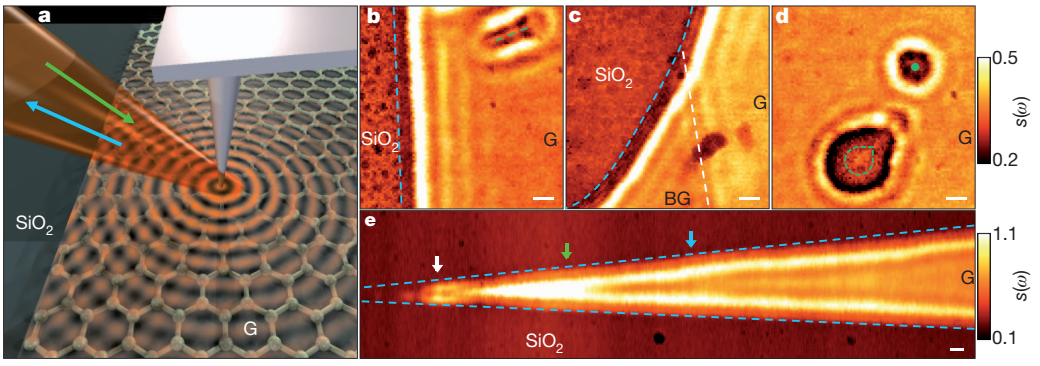


Figure 1 | Infrared nano-imaging experiment and results. a, Diagram of an infrared nano-imaging experiment at the surface of graphene (G) on SiO_2. Green and blue arrows display the directions of incident and back-scattered light, respectively. Concentric red circles illustrate plasmon waves launched by the illuminated tip. **b**–**e**, Images of infrared amplitude s ($\omega = 892\ cm^{-1}$) defined in the text taken at zero gate voltage. These images show a characteristic interference pattern close to graphene edges (blue dashed lines) and defects (green dashed lines and green dot), and at the boundary between single (G) and bilayer (BG) graphene (white dashed line). Additional features marked with arrows in **e** are analysed in refs 27 and 30. Locations of boundaries and defects were determined from AFM topography taken simultaneously with the near-field data. Scale bars, 100 nm. All data were acquired at ambient conditions.

[1]Department of Physics, University of California, San Diego, La Jolla, California 92093, USA. [2]Department of Physics and Astronomy, University of California, Riverside, California 92521, USA. [3]Materials Research Science and Engineering Center, University of Maryland, College Park, Maryland 20742, USA. [4]Department of Physics, Boston University, Boston, Massachusetts 02215, USA. [5]Department of Chemistry and Biochemistry, University of California, San Diego, La Jolla, California 92093, USA. [6]Department of Physics, California State University, San Marcos, California 92096, USA. [7]Graphene Research Centre and Department of Physics, National University of Singapore, 117542, Singapore. [8]Max Planck Institute of Quantum Optics and Center for Nanoscience, 85714 Garching, Germany.

©2012 Macmillan Publishers Limited. All rights reserved

third-order demodulated harmonics of the near-field amplitude measured for the given sample and for a Si reference sample, respectively[13]. The near-field amplitude $s(\omega)$ tracks real-space variations in the local electric field underneath the tip, enabling exploration of surface phonon polaritons and surface plasmons[15,16].

In Fig. 1b, we present a $s(\omega)$ image acquired at the graphene–SiO_2 interface revealing periodic oscillations of the $s(\omega)$ signal extending along the graphene edge. Point and circular defects (Fig. 1d) trigger circular fringe patterns. Line defects (Fig. 1b) produce elongated, elliptical patterns. Furthermore, we observed fringes at both sides of the boundary between single-layer and bilayer graphene (Fig. 1c). Finally, strongly tapered corners of graphene (Fig. 1e) reveal the two groups of fringes oriented along both edges of graphene in the field of view. In all cases, the periodicity of the fringe patterns is around 100 nm.

Images in Fig. 1 are consistent with the following scenario. Illuminated by focused infrared light, the AFM tip launches plasmon waves of wavelength λ_p propagating radially outward from the tip. Sample edges or defects act as (imperfect) reflectors of the plasmon waves, directing them back to the tip. Therefore complex patterns of interference between launched and reflected plasmons should form inside graphene. We emphasize that our experimental technique does not capture instantaneous snapshots of these complex patterns. Instead, whereas the tip 'launches' plasmon waves propagating in all directions, it only 'detects' the cumulative near-field plasmonic signal arising underneath it. This stands in rough analogy with the operating principle of sonar echolocation. In the top panels of Fig. 2a, we sketch the plasmon interference pattern in the form of plasmon amplitude, revealing standing wave oscillations between the tip and sample edge. As the tip is scanned towards the edge, it registers these oscillations with periodicity given by $\lambda_p/2$, as shown in the bottom panels of Fig. 2a. Our plasmon interference interpretation is supported by theoretical estimates of the wavelength λ_p. The plasmon dispersion of a two-dimensional metal residing at the interface of vacuum (dielectric constant $\varepsilon_0 = 1$) and a substrate with dielectric function $\varepsilon_{sub}(\omega)$ is given by the formula:

$$q_p = \frac{i\omega\kappa}{2\pi\sigma} \quad (1)$$

where $\kappa(\omega) = \kappa_1 + i\kappa_2 \equiv [\varepsilon_0 + \varepsilon_{sub}(\omega)]/2$ represents the complex effective dielectric function of the environment for graphene. Assuming that the conductivity (σ) of graphene takes a Drude form with relaxation time τ, equation (1) can be rewritten as:

$$q_p = \frac{\hbar^2\kappa(\omega)}{2e^2E_F}\omega(\omega + \frac{i}{\tau}) \quad (2)$$

where $\hbar$ is the reduced Planck's constant, e is the elementary charge, and E_F is the Fermi energy. Derivation of these equations and further refinements are discussed in the Supplementary Information. The real part of $q_p = q_1 + iq_2$ determines the plasmon wavelength $\lambda_p = 2\pi/q_1$, and the ratio between the imaginary part and the real part defines the plasmon damping rate $\gamma_p = q_2/q_1$. In graphene, the Dirac-like dispersion of the Fermi energy $E_F = \hbar v_F k_F$ with Fermi momentum $k_F = \sqrt{\pi|n|}$ (ref. 8) implies $|n|^{-1/2}$ scaling of the plasmon momentum with the carrier density n at fixed ω. Here $v_F \approx c/300 = 10^6\ m\ s^{-1}$ is the Fermi velocity. Finally, using frequency $\omega = 892\ cm^{-1}$ and $n \approx 8 \times 10^{12}\ cm^{-2}$ determined from the micro-Raman probe (see below) at the graphene edge, we find $\lambda_p \approx 200$ nm from equation (2), which is roughly twice the distance between fringes in Fig. 1b–e.

The images in Fig. 1b–e contain rich insights into processes governing plasmon propagation and losses on the surface of graphene. It is therefore instructive to examine line profiles along the direction normal to the sample edges. In Fig. 2b we show a plot obtained by averaging 150 such profiles—a procedure used to improve the signal-to-noise ratio. We find that the fringe widths increase from the interior to the edge of graphene, implying that the plasmon wavelength λ_p likewise increases. This behaviour is due to enhancement of the carrier density n near the sample edge, which is verified by our micro-Raman experiments (Fig. 2b inset)[17,18]. Thus, plasmonic interference patterns reported in Fig. 2b uncover the usefulness of infrared imaging for the nanoscale determination of local carrier density in graphene. In Fig. 2b we also show modelling results of plasmon profiles following a procedure detailed in the Supplementary Information. Our modelling provides a quantitative account of plasmon interferometry data. The carrier density profile (red curve in Fig. 2b inset) and the damping rate γ_p constitute the adjustable parameters of the model. Because plasmons in our experiments are launched and detected by the same point source (the AFM tip), the interference amplitude necessarily exhibits decay from the sample edge even when the damping rate is assumed to be vanishingly small (green trace in Fig. 2b). The best fit to the amplitude profile is achieved for significantly stronger damping, with $\gamma_p = 0.135$.

According to equations (1) and (2), the plasmon wavelength λ_p is directly determined by the carrier density n. We demonstrate this

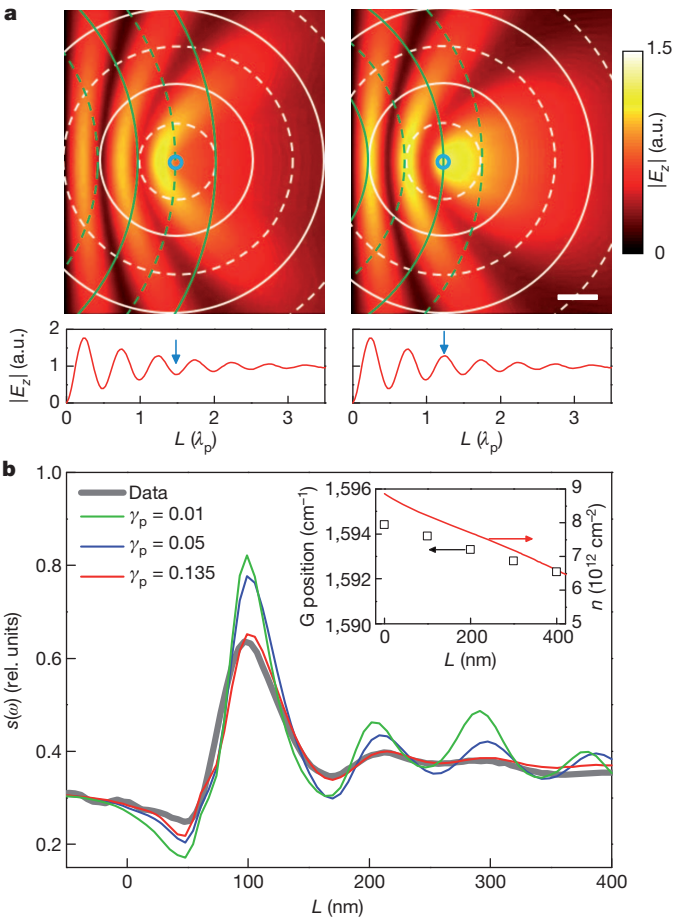


Figure 2 | Spatial variation of the electric field and near-field amplitude at the graphene edge. For all panels, graphene is present at $L > 0$, and SiO_2 not covered by graphene is displayed at $L < 0$. **a**, Upper panels, illustration of interference between tip-launched plasmon waves (white) and their reflection (green) from the edge at $L = 0$. Solid and dashed lines correspond to positive and negative field maxima of the propagating plasmon, respectively. False colour plots of the absolute value of electric field $|E_z|$ reveal standing waves formed between the tip and the edge. Left and right panels show snapshots of destructive (minimum signal) and constructive (maximum signal) interference underneath the tip, respectively. Scale bar, $0.5\lambda_p$. Lower panels, profiles of $|E_z|$ underneath the tip versus its distance to the edge. The blue circles and arrows mark the positions of the tip. **b**, Experimental (grey) and calculated (colour) $s(\omega)$ line profiles at zero gate voltage. Inset, G-peak positions inferred from micro-Raman data (squares) and the carrier density profile (red line) we used to model the plasmonic standing wave (in **b**). The Raman G-peak positions are associated with the variation of the local carrier density in graphene (n: right-hand scale)[17,18,29].

©2012 Macmillan Publishers Limited. All rights reserved

unique aspect of graphene plasmonics experimentally through imaging under gate bias (Fig. 3a). Over a range of V_g (gate voltage) values from +30 V to −20 V, the hole density n in our samples increases monotonically, a consequence of significant unintentional hole doping present even in ungated graphene/SiO_2/Si structures (Fig. 2b inset). This tuning of carrier density produces systematic variations in the plasmonic profiles: fringe amplitude and periodicity are both enhanced with increasing n. By inferring λ_p directly from the fringe width, we observe a systematic decrease in λ_p with the reduction in hole density. Our gate-dependent data for λ_p approximately follow the $\lambda_p \propto |n|^{1/2}$ law predicted for monolayer graphene[19]. In contrast, the plasmon damping rate does not show clear gate dependence and is roughly equal to 0.135 ± 0.015 at all V_g. This magnitude of γ_p significantly exceeds theoretical estimates for graphene with similar electronic mobility, $\mu \approx 8{,}000\ cm^2\ V^{-1}s^{-1}$ (ref. 12).

It is important to understand why plasmon damping in our structures is abnormally strong. According to equations (1) and (2), two additive contributions define damping rate as $\gamma_p \approx (\sigma_1/\sigma_2) + (\kappa_2/\kappa_1)$. The first term is associated with plasmonic losses inherent in graphene, whereas the second term describes losses due to the SiO_2 substrate. At $\omega = 892\ cm^{-1}$, we estimate $\kappa = 2.52 + 0.13i$ and hence, $\kappa_2/\kappa_1 \approx 0.05$, based on our ellipsometric measurements of SiO_2/Si wafers. The resulting value of $\sigma_1/\sigma_2 \approx 0.08$ is unexpectedly high, being three to four times higher than the estimate of $\sigma_1/\sigma_2 = (\omega\tau)^{-1}$ obtained from equation (2) using the relaxation rate $\tau^{-1} \approx 20\ cm^{-1}$, corresponding to a typical d.c. mobility of our samples. This discrepancy has two possible interpretations. Excessive losses may originate from an enhanced electronic relaxation rate at infrared frequencies compared to that established in d.c. transport. Alternatively, losses may be unrelated to free carrier mobility/dynamics and may instead be associated with extrinsic factors such as surface irregularities. Our plasmonic interferometry data in Figs 2 and 3 provide strong support for the former hypothesis. Indeed, these images yield γ_p and λ_p (Fig. 3b) and thus allow us to determine the complex optical conductivity of graphene (Fig. 3b inset) based on the following formulae: $\sigma_2 \approx \frac{\omega\kappa}{4\pi^2}\lambda_p$; $\sigma_1 = \sigma_2(\gamma_p - \kappa_2/\kappa_1)$. We remark that these relations between plasmonic parameters (λ_p, γ_p) and the complex optical conductivity σ of graphene hold true for any plasmonic material for which $\sigma_1 \ll \sigma_2$. Therefore these expressions apply even if the frequency-dependent conductivity deviates from the simple Drude model. The appeal of this analysis lies in establishing a link between real-space plasmonic profiles and the optical constants inferred from conventional infrared spectroscopy.

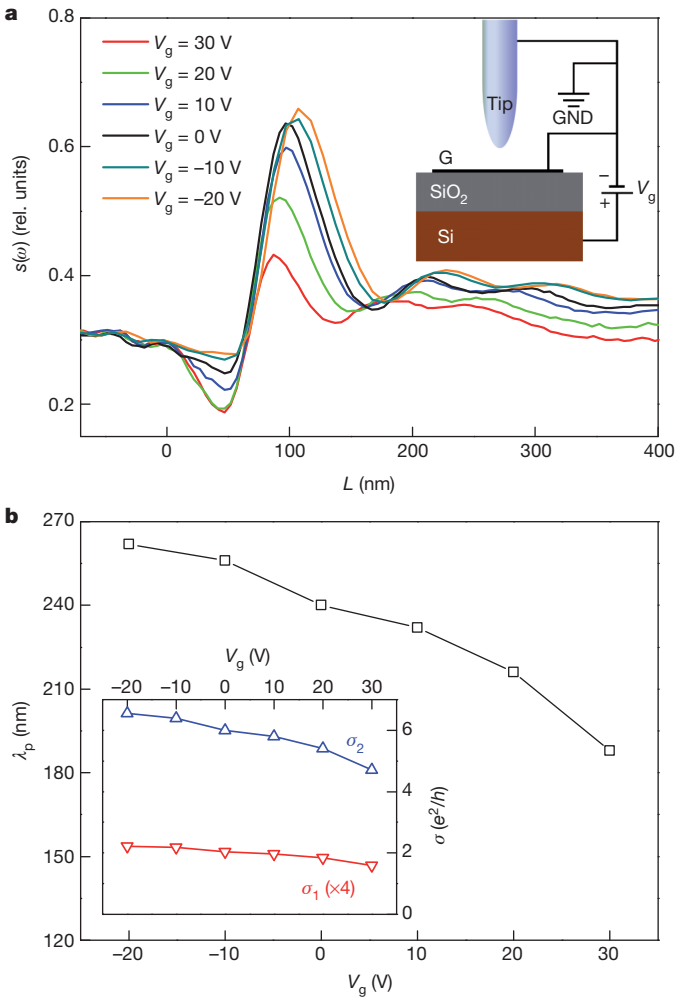


Figure 3 | Electrostatically tunable plasmons in back-gated graphene. **a**, Line profiles of $s(\omega)$ perpendicular to the graphene edge at various gate voltages, V_g. Inset, our gate bias set-up. Both the metalized tip and graphene are at ground (GND) potential. **b**, Gate-dependent plasmon wavelength λ_p. Inset, σ_1 and σ_2 of graphene at various gate voltages, estimated from λ_p and γ_p, as described in the text. These conductivity data show directly that the infrared response of graphene is predominantly reactive, $\sigma_2 \gg \sigma_1$, thus fulfilling an essential precondition for excitation of plasmons.

Our imaging data reveal that the real part of the conductivity of graphene is as high as $\sigma_1 \approx 0.5e^2/h$. This value greatly exceeds the theoretical estimate of σ_1 ($\omega = 892\ cm^{-1}$, $n = 8 \times 10^{12}\ cm^{-2}$, $\tau^{-1} = 20\ cm^{-1}$) $= 0.13e^2/h$ obtained from a model of non-interacting Dirac quasiparticles weakly scattered by disorder[20–22], but is comparable to infrared spectroscopy results for back-gated graphene on SiO_2/Si (ref. 10). In an ideal, non-interacting graphene, $\sigma_1(\omega < 2E_F)$ is vanishingly small owing to the phenomenon of 'Pauli blocking'[10]. Thus the source of strong plasmonic losses in our back-gated samples is traced to the unexpectedly large magnitude of σ_1. This result supports the notion of prominent many-body effects in graphene beyond the picture of non-interacting Dirac fermions[23–25]. Further experiments on suspended graphene, as well as devices using various types of dielectric substrates (such as hexagonal boron nitride), are needed to disentangle the roles of electron–electron and graphene–substrate interactions in the dissipation we observe at infrared frequencies. Our work uncovers an experimental path and analysis methodology for these future studies of many-body interactions in graphene.

Infrared nano-imaging experiments reported here have established graphene/SiO_2/Si structures as a potent plasmonic medium that enables voltage control of both the wavelength and the amplitude of the plasmons. Higher gate voltages than used in our study will allow for the binary on/off switching of plasmon propagation with a possibility of potentially local control by a top gate or a biased tip. The plasmon wavelength in graphene, $\lambda_p \approx 200$ nm, is one of the shortest imaged for any material, whereas the propagation length is on a par with Au in experiments monitoring strongly confined plasmons launched by AFM tips[16]. An important figure of merit, $\lambda_{IR}/\lambda_p = 50$–$60$, for our back-gated devices surpasses that of conventional Ag-based structures[12]. Intrinsic plasmonic losses in graphene that we analysed in detail can be substantially reduced or even eliminated through population inversion[26]. We stress that plasmon tuning is realized here in the architecture of a metal-oxide-semiconductor device (we used graphene-oxide-silicon), which is a ubiquitous system in modern information processing. Furthermore, the performance of even the first generation of plasmonic devices reported here and in ref. 27 is rather promising compared to non-tunable metal-based structures[12]. For all these reasons, we believe that graphene may be an ideal medium for active infrared plasmonics.

METHODS SUMMARY

Infrared nano-imaging. Our scattering-type SNOM apparatus (Neaspec) is based on an AFM operating in tapping mode. Measurements were performed at an AFM tapping frequency of $\Omega = 270$ kHz and a tapping amplitude of 40 nm. The shaft of the conducting AFM tip acts as an antenna that boosts the efficiency of

©2012 Macmillan Publishers Limited. All rights reserved

near-field interaction[28]. The back-scattered signal registered by the detector is strongly dependent on the tip–sample distance. This enables isolation of the genuine near-field contribution from the overall back-scattered signal, which is periodically modulated at harmonics of the tapping frequency Ω. The mth harmonic component of this signal $s_m \exp(i\phi_m)$, termed the mth demodulated signal (here $m = 3$), represents the desired near-field contribution.

Samples and devices. Our graphene samples were obtained by mechanical cleavage of bulk graphite and then transferred to SiO_2/Si substrate. To avoid surface contamination by lithographic procedures, bulk graphite connected to our graphene sample was used as an electrode in our back-gating experiments. To verify the gating functionality of our devices, we first performed a spectroscopic study of the hybrid plasmon–phonon resonance at various gate voltages and found good agreement with the published data[13]. Transport measurements of graphene samples fabricated following identical procedures indicate that the typical mobility of our graphene samples is about 8,000 $cm^2 V^{-1} s^{-1}$. Plasmon imaging experiments were completed for more than 30 graphene samples. All these structures exhibited highly reproducible behaviour and consistent values for the plasmon wavelength and damping. The data displayed in Figs 1–3 were obtained for devices with some of the weakest damping, revealing the largest number of plasmonic oscillations. Nevertheless, even in these devices the plasmonic losses are stronger than expectations based on typical electronic mobility measurements.

Micro-Raman measurements. According to previous studies, the position of the G-peak in the Raman spectrum of graphene is directly linked to its carrier density[17,18,29]. Therefore, the G-peak profile shown in Fig. 2b inset reflects the range of the variation in graphene carrier density close to the edge[17–19]. Our micro-Raman experiments were carried out using a Renishaw inVia Raman microscope equipped with a 50×, NA = 0.75 long-distance objective, a 1,800 lines per mm grating and an XY stage with a resolution of 100 nm. The spot size in these experiments is limited by diffraction. Therefore, the fragment of the line profile of the G-peak frequency shown in Fig. 2b inset is instrumentally broadened.

Received 29 February; accepted 17 May 2012.
Published online 20 June 2012.

1. Atwater, H. A. The promise of plasmonics. *Sci. Am.* **296,** 56–62 (2007).
2. West, P. R. *et al.* Searching for better plasmonic materials. *Laser Photon. Rev.* **4,** 795–808 (2010).
3. Stockman, M. I. Nanoplasmonics: the physics behind the applications. *Phys. Today* **64,** 39–44 (2011).
4. Maier, S. A. *Plasmonics: Fundamentals and Applications* Ch. 4 (Springer, 2007).
5. Schuller, J. A. *et al.* Plasmonics for extreme light concentration and manipulation. *Nature Mater.* **9,** 193–204 (2010).
6. Nagpal, P., Lindquist, N. C., Oh, S.-H. & Norris, D. J. Ultrasmooth patterned metals for plasmonics and metamaterials. *Science* **325,** 594–597 (2009).
7. Lal, S., Link, S. & Halas, N. J. Nano-optics from sensing to waveguiding. *Nature Photon.* **1,** 641–648 (2007).
8. Castro Neto, A. H., Guinea, F., Peres, N. M. R., Novoselov, K. S. & Geim, A. K. The electronic properties of graphene. *Rev. Mod. Phys.* **81,** 109–162 (2009).
9. Wang, F. *et al.* Gate-variable optical transitions in graphene. *Science* **320,** 206–209 (2008).
10. Li, Z. Q. *et al.* Dirac charge dynamics in graphene by infrared spectroscopy. *Nature Phys.* **4,** 532–535 (2008).
11. Vakil, A. & Engheta, N. Transformation optics using graphene. *Science* **332,** 1291–1294 (2011).
12. Jablan, M., Buljan, H. & Soljacic, M. Plasmonics in graphene at infrared frequencies. *Phys. Rev. B* **80,** 245435 (2009).
13. Fei, Z. *et al.* Infrared nanoscopy of Dirac plasmons at the graphene-SiO_2 interface. *Nano Lett.* **11,** 4701–4705 (2011).
14. Ju, L. *et al.* Graphene plasmonics for tunable terahertz metamaterials. *Nature Nanotechnol.* **6,** 630–634 (2011).
15. Huber, A., Ocelic, N., Kazantsev, D. & Hillenbrand, R. Near-field imaging of mid-infrared surface phonon polariton propagation. *Appl. Phys. Lett.* **87,** 081103 (2005).
16. Dallapiccola, R., Dubois, C., Gopinath, A., Stellacci, F. & Dal Negro, L. Near-field excitation and near-field detection of propagating surface plasmon polaritons on Au waveguide structures. *Appl. Phys. Lett.* **94,** 243118 (2009).
17. Casiraghi, C. *et al.* Raman spectroscopy of graphene edges. *Nano Lett.* **9,** 1433–1441 (2009).
18. Caridad, J. M. *et al.* Effects of particle contamination and substrate interaction on the Raman response of unintentionally doped graphene. *J. Appl. Phys.* **108,** 084321 (2010).
19. Hwang, E. H. & Das Sarma, S. Dielectric function, screening, and plasmons in two-dimensional graphene. *Phys. Rev. B* **75,** 205418 (2007).
20. Ando, T., Zheng, Y. & Suzuura, H. Dynamical conductivity and zero-mode anomaly in honeycomb lattices. *J. Phys. Soc. Jpn* **71,** 1318–1324 (2002).
21. Peres, N. M. R., Guinea, F. & Castro Neto, A. H. Electronic properties of disordered two-dimensional carbon. *Phys. Rev. B* **73,** 125411 (2006).
22. Gusynin, V. P. & Sharapov, S. G. Transport of Dirac quasiparticles in graphene: Hall and optical conductivities. *Phys. Rev. B* **73,** 245411 (2006).
23. Grushin, A. G., Valenzuela, B. & Vozmediano, M. A. H. Effect of Coulomb interactions on the optical properties of doped graphene. *Phys. Rev. B* **80,** 155417 (2009).
24. Peres, N. M. R., Ribeiro, R. M. & Castro-Neto, A. H. Excitonic effects in the optical conductivity of gated graphene. *Phys. Rev. Lett.* **105,** 055501 (2010).
25. Hwang, J., Leblanc, J. P. F. & Carbotte, J. P. Optical self-energy in graphene due to correlations. *J. Phys. Condens. Matter* **24,** 245601 (2012).
26. Rana, F. Graphene terahertz plasmon oscillators. *IEEE Trans. Nanotechol.* **7,** 91–99 (2008).
27. Chen, J. *et al.* Optical nano-imaging of gate-tunable graphene plasmons. *Nature* http://dx.doi.org/10.1038/nature11254 (this issue).
28. Novotny, L. & Hecht, B. *Principles of Nano-Optics* (Cambridge Univ. Press, 2006).
29. Das, A. *et al.* Monitoring dopants by Raman scattering in an electrochemically top-gated graphene transistor. *Nature Nanotechnol.* **3,** 210–215 (2008).
30. Rodin, A. S. *Electronic Properties of Low-Dimensional Systems.* PhD thesis, UCSD (2012).

Supplementary Information is linked to the online version of the paper at www.nature.com/nature.

Acknowledgements We acknowledge support from AFOSR, ONR and DARPA. The analysis of plasmonic losses and many-body effects was supported by DOE-BES grant DE-FG02-00ER45799. W.B., Z.Z. and C.N.L. were supported by NSF DMR/1106358, ONR N00014-09-1-0724, ONR/DMEA H94003-10-2-1003 and FENA Focus Center. G.D. and M.T. were supported by NASA. M.M.F. was supported by UCOP and NSF PHY11-25915. A.H.C.N. acknowledges NRF-CRP grant R-144-000-295-281. L.M.Z was supported by DOE grant no. DE-FG02-08ER46512. M.W. thanks the Alexander von Humboldt Foundation for financial support. F.K. was supported by Deutsche Forschungsgemeinschaft through the Cluster of Excellence Munich Centre for Advanced Photonics.

Author Contributions All authors were involved in designing the research, performing the research, and writing the paper.

Author Information Reprints and permissions information is available at www.nature.com/reprints. The authors declare competing financial interests: details accompany the full-text HTML version of the paper at www.nature.com/nature. Readers are welcome to comment on the online version of this article at www.nature.com/nature. Correspondence and requests for materials should be addressed to D.N.B. (dbasov@physics.ucsd.edu).

©2012 Macmillan Publishers Limited. All rights reserved

doi:10.1038/nature11253

I. ORIGIN OF THE OBSERVED SPATIAL MODULATIONS

The qualitative explanation of the observed interference patterns is as follows. The tip of the near-field nanoscope excites a circular surface plasmon. A complex pattern of interference between the launched plasmon and its reflection off the sample edges is formed, as sketched in Fig. 1 of the main text. The signal $s(x, y)$ detected by the nanoscope is proportional to the plasmonic amplitude directly underneath the tip, i.e., at the same in-plane point (x, y).

For simplicity, let us treat graphene as a half-infinite homogeneous medium. Denote by $A(r)$ be the complex amplitude of a circular wave at a distance r from its origin that would be excited in an infinite sample. Function $A(r)$ oscillates with plasmon momentum q_1 and decays as $\sim e^{-q_2 r}$ at large r due to damping. According to the method of images, for our half-infinite sample (with the edge at $x = 0$) the near-field amplitude registered by the tip is given by

$$s(x, y) \propto |A(0) + e^{i\theta} A(2x)| \,. \tag{S1}$$

Here the term $A(0)$ is due to the tip-launched wave, the term $e^{i\theta} A(2x)$ is due to its image, i.e., the reflected wave, and θ is the phase shift upon reflection (a number close to π). The interference underneath the tip is constructive at

$$x_j = \frac{\lambda_p}{2} \left(j - \frac{\theta}{2\pi} \right) , \quad j = 1, 2, \ldots \tag{S2}$$

This condition implies that the interference fringes are straight lines parallel to the edge. The distance between adjacent fringes is one half of the plasmon wavelength $\lambda_p \equiv 2\pi/q_1$. The first fringe at $x = x_1$ is expected to be the strongest. The amplitude of the subsequent fringes should monotonically decrease because the total amount of damping grows with the roundtrip distance $2x_j$.

The described physical picture is sufficient for a qualitative explaination of our experiments. In the remaining sections we develop it into a quantitative model by properly taking into account response functions of graphene and its SiO_2 substrate, as well as the interaction between the tip and the sample.

II. MOMENTUM AND FREQUENCY DEPENDENCE OF GRAPHENE CONDUCTIVITY

Within the linear-response theory, in-plane electric field $\tilde{\mathbf{E}}_\parallel$ and current density $\tilde{\mathbf{j}}$ in graphene are related by the momentum and frequency dependent conductivity $\sigma(q,\omega)$:

$$\tilde{\mathbf{j}}(q,\omega) = \sigma(q,\omega)\tilde{\mathbf{E}}_\parallel(q,\omega)\,. \tag{S3}$$

(Here and below the tilde marks the Fourier transforms.) In this section we summarize the main properties of function $\sigma(q,\omega)$ and clarify assertions made about it in the main text.

The conductivity of the two-dimensional (2D) electron gas in graphene is related to its polarization function $P(q,\omega)$ by $\sigma(q,\omega) = ie^2(\omega/q^2)P(q,\omega)$. The formula for $P(q,\omega)$ has been derived within the random-phase approximation for zero temperature and no disorder.[1,2] We assume that the latter can be introduced by replacing ω with $\zeta = \omega + i\tau^{-1}$, where τ is the phenomenological relaxation time. In this way, we arrive at

$$\sigma(q,\omega) = \sigma_0(q,\omega)\left[1 + \mathcal{G}\left(\frac{\hbar\zeta + 2E_F}{\hbar v q}\right) - \mathcal{G}\left(\frac{\hbar\zeta - 2E_F}{\hbar v q}\right)\right] - \frac{2i}{\pi}\frac{e^2\omega E_F}{(\hbar v q)^2}\,, \tag{S4}$$

where

$$\sigma_0(q,\omega) = -i\frac{e^2}{4\hbar}\frac{\zeta}{\sqrt{v^2q^2 - \zeta^2}} \tag{S5}$$

is the conductivity of undoped graphene and function $\mathcal{G}(\alpha)$ is defined by

$$\mathcal{G}(\alpha) = -\frac{1}{\pi}\left(\alpha\sqrt{1-\alpha^2} - \arccos\alpha\right)\,. \tag{S6}$$

In our model and simulations we neglect the momentum dependence of $\sigma(q,\omega)$. This is justified in the $q \ll \omega/v$ limit, where Eq. (S4) simplifies to[1]

$$\sigma(\omega) = \frac{i}{\pi}\frac{e^2}{\hbar}\left[\frac{1}{\bar{\zeta}} - \frac{1}{4}\ln\left(\frac{2+\bar{\zeta}}{2-\bar{\zeta}}\right)\right]\,, \quad \bar{\zeta} = \frac{\hbar\zeta}{E_F}\,. \tag{S7}$$

The disappearance of the q-dependence means that quasiparticles perceive the perturbing electric field as locally uniform. This is because the quasiparticle displacement $2\pi v/\omega$ over the time period of the field is much smaller than its wavelength $2\pi/q$.

If, in addition to $q \ll \omega/v$, the condition $\hbar\omega \ll E_F$ is also met, so that $\bar{\zeta} \ll 1$, Eq. (S7) reduces to the Drude-like formula

$$\sigma(\omega) = \frac{e^2}{\pi\hbar^2}\frac{E_F\tau}{1 - i\omega\tau}\,, \tag{S8}$$

which was used in Eq. (2) of the main text.

III. LOCAL APPROXIMATION FOR GRAPHENE RESPONSE

The characteristic in-plane momenta q relevant in our experiments are of the order of the plasmon momentum

$$q_p = i\kappa\omega/(2\pi\sigma) \tag{S9}$$

[same as q_p in Eq. (1) of the main text]. It can be verified that such momenta satisfy the conditions $q \ll k_F, \omega/v_F$. As explained in Sec. II above, in this case the q-dependence of the conductivity can be neglected. Equation (S3) can therefore be replaced by the simplified local relation

$$\mathbf{j}(\mathbf{r}) = \sigma(\mathbf{r})\mathbf{E}_\parallel(\mathbf{r})\,, \quad \mathbf{E}_\parallel(\mathbf{r}) = -\nabla\Phi(\mathbf{r})\,, \quad \nabla \equiv (\partial/\partial x, \partial/\partial y)\,, \tag{S10}$$

which is valid even for systems without translational invariance. Below we use this relation to derive a closed system of equations that describe the response of graphene to an arbitrary external potential $\Phi_{\text{ext}}(\mathbf{r})$.

Within the quasi-static approximation, valid if all distances of interest are much shorter than the optical wavelength $2\pi c/\omega$, the total *in-plane* potential $\Phi(\mathbf{r})$ is given by

$$\Phi(\mathbf{r}) = \Phi_{\text{ext}}(\mathbf{r}) + V(\mathbf{r},0) * \delta\rho(\mathbf{r})\,, \quad V(\mathbf{r},z) = \frac{1}{\kappa}\frac{1}{\sqrt{|\mathbf{r}|^2+z^2}}\,, \tag{S11}$$

where κ is defined in Eq. (1) of the main text, the star denotes convolution,

$$(A * B)(\mathbf{r}) \equiv \int d^2\mathbf{r}' A(\mathbf{r}-\mathbf{r}')B(\mathbf{r})\,, \tag{S12}$$

and $\delta\rho(\mathbf{r})$ is the charge density induced in graphene. Combining Eqs. (S10), (S11), and the continuity relation, $-i\omega\delta\rho + \nabla\mathbf{j} = 0$, we get the single equation for $\Phi(\mathbf{r})$:

$$\Phi(\mathbf{r}) + \frac{\kappa}{2\pi} V(\mathbf{r},0) * \left(\nabla q_p^{-1}(\mathbf{r})\nabla\Phi\right) = \Phi_{\text{ext}}(\mathbf{r})\,. \tag{S13}$$

In general, it has to be solved numerically. The analytical solution can be obtained for an infinite system of constant σ using the Fourier transform method, which yields

$$\tilde{\Phi}(\mathbf{q}) = \frac{q_p}{q_p - |\mathbf{q}|}\,\tilde{\Phi}_{\text{ext}}(\mathbf{q})\,. \tag{S14}$$

The plasmon momentum q_p correspond to the poles of $\tilde{\Phi}(\mathbf{q})$ in the complex-q plane.

Consider, in particular, the external potential

$$\Phi_d(\mathbf{r}) = \frac{1}{\kappa}\frac{z_d}{(|\mathbf{r}-\mathbf{r}_d|^2+z_d^2)^{3/2}}\,, \quad \tilde{\Phi}_d(\mathbf{q}) = \frac{2\pi}{\kappa}\,e^{-i\mathbf{q}\mathbf{r}_d - |\mathbf{q}|z_d} \tag{S15}$$

created by a unit dipole located at $(\mathbf{r}_d, z_d)$. Later we will need an expression for the electric field $\mathbf{E}_g = (\mathbf{E}_{g,\parallel}, E_{g,z})$ induced by electrons in graphene at an arbitrary point in space $(\mathbf{r}_c, z_c)$ in response to this dipole:

$$\mathbf{E}_{g,\parallel}(\mathbf{r}_c, z_c) = -\nabla_{\mathbf{r}_c}\big(V(\mathbf{r}, z_c) * \delta\rho\big)(\mathbf{r}_c)\,, \quad E_{g,z}(\mathbf{r}_c, z_c) = -\frac{\partial}{\partial z_c}\big(V(\mathbf{r}, z_c) * \delta\rho\big)(\mathbf{r}_c)\,. \tag{S16}$$

Using Eqs. (S14), (S15), and (S16), we find

$$E_{g,z}(\mathbf{r}_d, z_d) = -\frac{1}{\kappa}\int\limits_0^\infty \frac{q^3 dq}{q_p - q}\, e^{-2qz_d}\,, \tag{S17}$$

as in our previous work.[3] The induced electric field has another contribution $\mathbf{E}_s$ from charges on the surface of the substrate. Using the method of images, we get

$$\mathbf{E}_s(\mathbf{r}_c, z_c) = \beta\,\frac{3(\hat{\mathbf{z}}\mathbf{R})\mathbf{R} - \hat{\mathbf{z}}R^2}{R^5}\,, \quad \beta = 1 - \frac{1}{\kappa}\,, \quad \mathbf{R} = (\mathbf{r}_c - \mathbf{r}_d, z_c + z_d)\,. \tag{S18}$$

Consider next a situation where graphene occupies $x \geq 0$ half-plane, which is relevant for s-SNOM imaging near the graphene edge. Equation (S13) is still valid if we define $\sigma(x < 0) \equiv 0$ and also add a boundary condition $\partial\Phi/\partial x = 0$ so that $j_x = 0$ at $x = 0$ to avoid infinite charge accumulation at the edge. Let us assume that $\sigma = \sigma(x)$ is invariant along y but may be a function of x. Without loss of generality, we can choose the dipole y-coordinate to be zero, $y_d = 0$. Taking the one-dimensional Fourier transform in y of both sides of Eq. (S13), we obtain

$$\tilde{\Phi}(x) - \frac{2}{\kappa}\,K_0(x|q_y|) * \delta\tilde{\rho}(x, q_y) = \tilde{\Phi}_d(x, q_y) = \frac{2}{\kappa}\,\frac{z_d}{r}\,|q_y|K_1(r|q_y|)\,, \tag{S19}$$

$$\delta\tilde{\rho}(x, q_y) = -\frac{\kappa}{2\pi}\left[\frac{d}{dx}\frac{1}{q_p(x)}\frac{d}{dx} - \frac{q_y^2}{q_p(x)}\right]\tilde{\Phi}(x, q_y)\,, \tag{S20}$$

where the convolution $(*)$ is now done along the x only, $r = \sqrt{(x - x_d)^2 + z_d^2}$, and $K_\nu(z)$ is the modified Bessel function of the second kind. The equations for the induced field become

$$E_{g,\alpha}(x_c, z_c) = \int\limits_0^\infty dx \int\limits_{-\infty}^\infty \frac{dq_y}{2\pi}\,\frac{2}{\kappa}\,\frac{u_\alpha}{r}\,|q_y|K_1(u|q_y|)\delta\tilde{\rho}(x, q_y)\,, \quad \alpha = \{x, z\}\,, \tag{S21}$$

where $u_x = x_c - L$, $u_z = z_c$, and $u = \sqrt{u_x^2 + u_z^2}$.

In our simulations we had to compute $E_{g,\alpha}$ numerically for a large number of collocation points (x_c, z_c) and source dipole positions (x_d, z_d). For this purpose, we converted the above integral equations into linear equations of a finite size. Instead of a semi-infinite plane, we

assumed that graphene occupies a strip $0 < x < 2w$ of a large width $2w$. We discretized the x coordinates and replaced all derivatives by finite differences. The convolution integral was replaced by an integral sum. A special care was taken to regularize the divergence of the modified Bessel functions at zero arguments by requiring that the convolution gives the same result for $\delta\tilde{\rho} = \text{const}$ whether it is computed numerically or analytically at all points of the x-grid. Similarly, we introduced a grid of q_y extending up to a suitably large value. Grid parameters were adjusted to ensure that the accuracy of our solution was never less than 1%. The sequence of steps involved in our numerical simulations is explained further in Sec. IV.

IV. TIP-SAMPLE COUPLING

The goal of the modeling was to understand the imaging contrast, i.e., relative variations of the scattering amplitude S measured by s-SNOM as a function the AFM tip position.

Fully realistic simulations of the tip-sample coupling are computationally prohibitive, and so we tried several approximations. The first approximation we considered was the conventional the point-dipole model.[4–6] This simple model did grasp some of the key characteristics of the imaging contrast. However, it came short of a quantitative account of the experimental data. Much better agreement was obtained using the model in which the AFM tip is approximated by a metallic spheroid.[7] The spheroid is defined by the equation

$$(x - L)^2 = \frac{a}{L_{\text{tip}}}(z - z_{\text{tip}})(2L_{\text{tip}} + z_{\text{tip}} - z)\,, \quad z_{\text{tip}} \le z \le z_{\text{tip}} + 2L_{\text{tip}}\,, \tag{S22}$$

where L is the x-coordinate of the tip, $2L_{\text{tip}}$ is its total length, and a is its radius of curvature at the ends. The desired scattering amplitude S is proportional to the total radiating dipole p_z of the spheroid. (For a strongly elongated spheroid, $L_{\text{tip}} \gg a$, its in-plane dipole moment is much smaller than p_z and can be neglected.) In order to compute p_z, we assume that the electric potential $\Phi_{\text{ext}}(\mathbf{r}, z)$ outside both the tip and the sample can be represented as a superposition of potentials of a large number N_d of point dipoles positioned inside the tip:

$$\Phi_{\text{ext}}(\mathbf{r}, z) = \sum_{j=1}^{N_d} p_j \Phi_d(\mathbf{r}_{d,j} - \mathbf{r}, z_{d,j} - z)\,. \tag{S23}$$

Using the formalism developed in Sec. III, we compute the full potential $\Phi(\mathbf{r}, z)$ and the corresponding electric field $\mathbf{E}(\mathbf{r}, z)$ at N_d collocation points $(x_{c,j}, z_{c,j})$ at the spheroid surface.

Imposing the boundary condition that the component of $\mathbf{E}(\mathbf{r}, z)$ tangential to this surface is zero, we obtain the system of linear equations for the individual dipole moments p_j. The total dipole moment p_z of the tip is their sum.

We tested this algorithm first on the case of infinite graphene, where the accuracy of the solution for p_z as a function of $z_{\rm tip}$, $L_{\rm tip}$, and a can be verified by independent numerical methods.[7] We found that accuracy better than 1% can be reached by working with $N_d \gtrsim 2L_{\rm tip}/a$ dipoles positioned equidistantly on the spheroid axis $z_{d,j} = z_{\rm tip} + (2L_{\rm tip}/N_d)(j-1/2)$. The z-coordinates of the collocation points were taken to coincide with those of the dipoles, $z_{c,j} = z_{d,j}$. Their x-coordinates were all chosen to be on the same side of L, i.e., $x_{c,j} > L$. The same sets of points were later used for the problem of the graphene strip. In principle, in this case the off-axis placement of the dipoles may be warranted and also both $x_{c,j} > L$ and $x_{c,j} < L$ should be considered. However, investigation of these issues requires time-consuming computations and so it is left for future work. In any case, for aspect ratios $L_{\rm tip}/a = 2$–10, we found our numerical results to be stable as long as N_d was about $2L_{\rm tip}/a$ or larger and at the same time the minimal distance between the tip and the sample was not smaller than $0.1a$. Regarding the latter, we note that although the distance between the tip and the sample can nominally be zero, the tip is covered by a Pt-Ir film with a skin depth $\sim 20\,$nm. Therefore, even in this case using some finite positive value for $z_{\rm tip}$ is physically justified in our electromagnetic calculations.

In the experiment the AFM is used in the tapping mode and the tapping harmonics $s_m e^{i\phi_m}$ are recorded. We modeled this by considering the time-dependent $z_{\rm tip}$ in the form

$$z_{\rm tip}(t) = z_{\rm min} + \Delta z\,(1 - \cos\Omega t)\,, \tag{S24}$$

Computing $S(t) \propto p_z(t)$ for a suitably dense grid of t-points and taking the discrete Fourier transform at frequency $m\Omega$, the desired demodulated amplitudes $s_m e^{i\phi_m}$ can be obtained.

The simulations proceed as follows. Given a profile of $q_p(x)$ (see Sec. V) and a pair of the tip coordinates $(L, z_{\rm tip})$, the matrices of the linear systems are generated as discussed above. These linear equations are solved and the magnitudes of the effective dipoles are computed. Their sum is taken to be the scattering amplitude S (up to an unimportant multiplicative constant). These calculations are repeated for a grid of tip positions L (typically, a hundred points) and heights $z_{\rm tip}$ (20 points). Upon demodulation, the spatial profile of $s_3(L)$ is computed. Normalizing it by s_3 calculated for the reference Si substrate (without graphene),

the relative amplitude $s(L)$ is obtained. These results are then utilized to fit the experimental data for $s(L)$ (Fig. 1 of the main text), as described in the next section.

V. DATA FITTING PROCEDURE

The input into our simulation consists of the tip modeling parameters a, $L_{\rm tip}$, $z_{\rm min}$, the known tapping amplitude $\Delta z = 40\,\mathrm{nm}$, the value of $\kappa(\omega = 892\,\mathrm{cm}^{-1}) = 2.52 + 0.13i$ (based on our ellipsometric measurements of SiO_2/Si wafers), and also the spatial profile of $q_p(L)$. (For notation consistency with Fig. 2c of the main text, we relabel x to L in this section.)

We fixed $a = 30\,\mathrm{nm}$, similar to our previous work.[3] We tried several $L_{\rm tip}/a$ ratios and found the results not to be very sensitive to this parameter, as long as it is large. We settled on $L_{\rm tip}/a = 9$ for numerical efficiency. For $q_p(L) = q_1(L) + iq_2(L)$ we adopted the polynomial form

$$q_1(x) = \sum_{j=0}^{6} a_j L^j\,, \quad q_2(L) = \gamma_p q_1(L)\,. \tag{S25}$$

For simplicity, the plasmon damping parameter γ_p was taken to be position-independent. The coefficients a_j were iteratively adjusted until a good agreement with the measured s_3-profile was obtained, see Fig. S1. The minor discrepancies between the experiments and simulations could be due to a systematic error introduced by the spheroid approximation (after all, the tip is not an ideal metallic spheroid) and the lack of perfect translational invariance of the system along the edge.

For ungated sample, $V_g = 0$, we made additional checks. The fitted $q_1(L)$ was converted into the profile of the carrier (in this case, hole) density $n(L)$ with the help of the relation

$$n(L) = \frac{1}{\pi}\, k_F^2(L)\,, \quad k_F(L) = \frac{\hbar\omega^2}{2e^2 v}\,\frac{|\kappa|}{q_1(L)}\,, \tag{S26}$$

which follows from Eqs. (S8) and (S9). This determination of $n(L)$ was verified by micro-Raman measurements. As one can see from Fig. 2c, both the magnitude of the carrier density increase toward the graphene edge and the length scale over which this increase occurs are consistent with the Raman data. In fact, the near-field and the Raman methods give complementary information about the local density. The former is most reliable in the range $0 < L \lesssim 400\,\mathrm{nm}$ while the latter is accurate at $L \gtrsim 1\,\mu\mathrm{m}$. These two groups of results

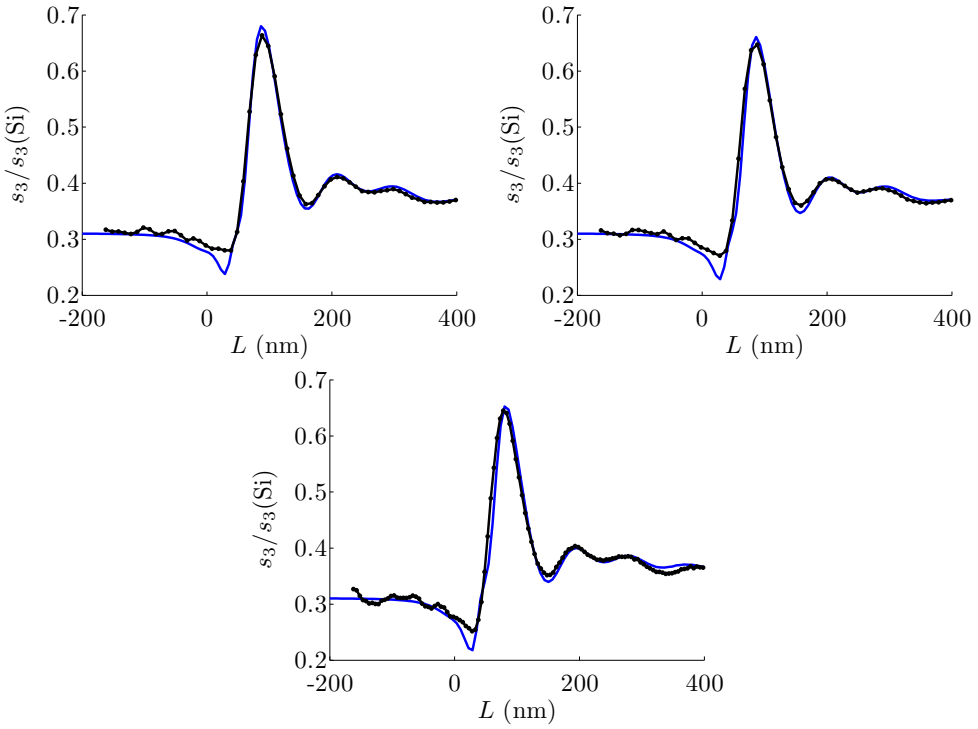


FIG. S1. The absolute value of the s-SNOM 3rd harmonics for gate voltages (clockwise from top left) $V_g = -20$, -10, and $0\,\mathrm{V}$. The black dots connected by the lines are the experimental data; the blue solid lines are the theoretical fits using $\gamma_p = 0.135$.

were interpolated by another polynomial function

$$n(L) = \sum_{j=0}^{6} c_j \left[L\,(\mathrm{nm})\right]^j \times (10^{12}\,\mathrm{cm}^{-2})\,, \tag{S27}$$

where $c_7 = -4.062191 \times 10^{-21}$, $c_6 = 2.999730 \times 10^{-17}$, $c_5 = -8.646941 \times 10^{-14}$, $c_4 = 1.210092 \times 10^{-10}$, $c_3 = -8.233038 \times 10^{-8}$, $c_2 = 2.506465 \times 10^{-5}$, $c_1 = -0.008350$, and $c_0 = 8.861376$. This interpolation is shown by the solid line in Fig. 2c of the main text.

[1] B. Wunsch, T. Stauber, F. Sols, and F. Guinea, New J. Phys. **8**, 318 (2006).

[2] E. H. Hwang and S. Das Sarma, Phys. Rev. B **75**, 205418 (2007).

[3] Z. Fei, G. O. Andreev, W. Bao, L. M. Zhang, A. S. McLeod, C. Wang, M. K. Stewart, Z. Zhao, G. Dominguez, M. Thiemens, M. M. Fogler, M. J. Tauber, A. H. Castro-Neto, C. N. Lau, F. Keilmann, and D. N. Basov, Nano Lett. **11**, 4701 (2011).

[4] R. Hillenbrand and F. Keilmann, Phys. Rev. Lett. **85**, 3029 (2000).

[5] T. Taubner, F. Keilmann, and R. Hillenbrand, Nano Lett. **4**, 1669 (2004).

[6] J. Aizpurua, T. Taubner, F. J. G. de Abajo, M. Brehm, and R. Hillenbrand, Opt. Express **16**, 1529 (2008).

[7] L. M. Zhang, G. O. Andreev, Z. Fei, A. S. McLeod, G. Dominguez, M. Thiemens, D. N. Basov, A. H. Castro Neto, and M. M. Fogler, Phys. Rev. B **85**, 075419 (2012).